Available online at www.sciencedirect.com

ScienceDirect

journal homepage: www.elsevier.com/locate/he

Binder-free bifunctional SnFe sulfide/oxyhydroxide heterostructure electrocatalysts for overall water splitting

Ting Zhang [a,b], *Jingyi Han* [b], *Tianmi Tang* [b], *Jianrui Sun* [a,**], *Jingqi Guan* [b,*]

[a] *School of Chemistry and Life Science, Changchun University of Technology, Changchun 130012, Jilin, China*
[b] *Institute of Physical Chemistry, College of Chemistry, Jilin University, 2519 Jiefang Road, Changchun, 130021, China*

HIGHLIGHTS

- $SnFeS_xO_y$/NF shows low HER overpotentials of 85 and 324 mV at 10 and 1000 mA cm^{-2}, respectively.
- $SnFeS_xO_y$/NF shows overpotential of only 281 mV at 100 mA cm^{-2} for the OER.
- $SnFeS_xO_y$/NF-based electrolyzer needs 1.69 V to deliver 50 mA cm^{-2}.
- Heterostructure between sulfides and oxyhydroxides improves the electrocatalytic activity.

GRAPHICAL ABSTRACT

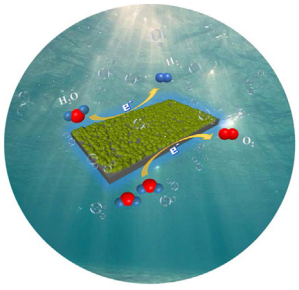

ARTICLE INFO

Article history:
Received 12 September 2022
Received in revised form
28 October 2022
Accepted 3 November 2022
Available online 23 November 2022

Keywords:
Sulfide
Oxyhydroxide
Hydrogen evolution reaction
Oxygen evolution reaction
Overall water splitting

ABSTRACT

Developing robust non-noble catalysts towards hydrogen evolution reaction (HER) and oxygen evolution reaction (OER) is vital for large-scale hydrogen production from electrochemical water splitting. Here, we synthesize Sn- and Fe-containing sulfides and oxyhydroxides anchored on nickel foam ($SnFeS_xO_y$/NF) using a solvothermal method, in which a heterostructure is generated between the sulfides and oxyhydroxides. The $SnFeS_xO_y$/NF exhibits low overpotentials of 85, 167, 249, and 324 mV at 10, 100, 500 and 1000 mA cm^{-2} for the HER, respectively, and a low overpotential of only 281 mV at 100 mA cm^{-2} for the OER. When it serves as both anode and cathode to assemble an electrolyzer, the cell voltage is only 1.69 V at 50 mA cm^{-2}. The sulfides should be the efficient active species for the HER, while the oxyhydroxides are highly active for the OER. The unique sulfide/oxyhydroxide heterostructure facilitates charge transfer and lowers reaction barrier, thus promoting electrocatalytic processes.

* *Corresponding author.*
** *Corresponding author.*
E-mail addresses: goodluck@ccut.edu.cn (J. Sun), guanjq@jlu.edu.cn (J. Guan).
https://doi.org/10.1016/j.ijhydene.2022.11.039

Introduction

To solve energy and environmental issues, hydrogen is considered as a promising alternative fuel owing to the high efficiency, cleanness, and renewability [1,2]. Electrochemical water splitting actuated by electricity from intermittent solar energy and wind energy sources is the cleanest way to produce high-purity hydrogen [3,4]. However, the energy efficiency is abidingly plagued by the thermodynamically uphill HER and OER processes, requiring high overpotentials to overcome the reaction barriers [5,6]. To address this dilemma, high-efficiency HER/OER electrocatalysts should be developed to reduce the overpotentials [7–9]. Although Pt-based materials and IrO_2 show outstanding HER and OER performance, respectively, the scarcity and high cost substantially hinder their widespread application [10,11]. To substitute noble metal catalysts with earth-abundant and economical catalysts, non-noble transition metal compounds such as carbides, nitrides, phosphates, sulfides, and oxyhydroxides have been exploited for the HER or OER in alkaline media [12]. Nevertheless, it is challenging to integrate the same catalyst as cathode and anode materials for overall water splitting due to inconsistent optimum running conditions [13,14]. Developing bifunctional HER and OER electrocatalysts can help to reduce catalyst preparation cost and makes hydrogen production from electrolysis of water more competitive than hydrogen production from fossil fuels [15]. However, most bifunctional electrocatalysts fail to reach 10 mA cm^{-2} at cell voltage of 1.5 V, worse than Pt–IrO_2-coupled electrolyzer [16,17]. Therefore, it is still challenging to fabricate bifunctional electrocatalysts for water electrolysis.

Binary metal oxyhydroxides usually show higher electrocatalytic OER activity than their unary counterparts ascribed to more appropriate binding energies of reaction intermediates on the catalyst surface, especially for Fe-based oxyhydroxides [18–22]. For instance, binary Fe–Co [23], Fe–Ni [24], Fe–Mn [25], Fe–Cu [26], and Fe–V [27] oxyhydroxides have been reported to exhibit excellent OER activity. Menezes et al. electrodeposited $FeSn_2$ on nickel foam (NF), showing excellent OER activity with an overpotential (η_{10}) of 197 mV at 10 mA cm^{-2} [28]. They proposed that the in situ generated α-FeOOH was the active site, while $FeSn_2$ provided conductive substrate. However, transition metal oxyhydroxides usually exhibit poor HER activity and the cell voltage would exceed 1.7 V at 10 mA cm^{-2} when they serve as bifunctional catalysts for water electrolysis [29]. Accordingly, coupling transition metal oxyhydroxides with high-efficiency HER catalysts is an efficient method for realizing overall water splitting [1,15,30,31].

Transition-metal sulfides have been demonstrated as high-performance catalysts for HER [15,32,33]. For example, MoS_2 [34], WS_2 [35], FeS [36], Co_9S_8 [37], and Ni_3S_2 [38] have been reported to be active for the HER. Wang et al. found that ultrathin metal-phase FeS nanosheets exhibited higher HER activity than the bulk FeS semiconductor due to enhanced carrier transfer [39]. Usually, binary metal sulfides exhibit higher HER activity than their unary counterparts mainly due to the formation of heterostructure between different sulfides and the generation of defects aroused by different valence states of metal ions [40]. Yan et al. found that the HER activity of NiS_2 can be greatly improved by doping Co ions [41]. They used theoretical simulations to disclose that the metal sites acted as the electron-reception centers, while the adsorbed water molecules were split on the surface sulfur sites. In addition, transition-metal sulfides also exhibit OER activity and heteroatom doping can further improve the catalytic performance due to the generation of defects and optimized surface electronic structure, leading to new charge distribution [42]. However, transition-metal sulfides are not stable under harsh oxidizing conditions, which would be partially or completely oxidized into the corresponding oxides [43]. Therefore, constructing a transition-metal sulfide/oxyhydroxide heterostructure catalyst is good choice to address the incompatibility between activity and stability.

Although transition-metal sulfides and transition-metal oxyhydroxides have been widely studied in HER and OER, respectively, there are seldom reports about establishing sulfide/oxyhydroxide heterostructure catalysts for bifunctional HER and OER. Here, we report a heterostructure catalyst containing $SnFeS_x$ and $SnFeO_y$ supported on nickel foam ($SnFeS_xO_y$/NF) through an in situ solvothermal method. For the HER, the $SnFeS_xO_y$/NF needs low overpotentials of 85, 167, 249, and 324 mV at 10, 100, 500 and 1000 mA cm^{-2}, respectively. For the OER, the $SnFeS_xO_y$/NF needs a low overpotential of only 281 mV at 100 mA cm^{-2}. Moreover, the electrolyzer using $SnFeS_xO_y$/NF as both anode and cathode needs a low cell voltage of 1.69 V to deliver 50 mA cm^{-2}. The formation of sulfide/oxyhydroxide heterostructure facilitates charge transfer and reduces OER barrier, thus enhancing electrocatalytic performance.

Results and discussion

The heterostructure catalyst $SnFeS_xO_y$/NF was synthesized in a solvothermal reaction using sulfourea as the sulfur source and $FeCl_3 \cdot 6H_2O$ and $SnCl_2 \cdot 2H_2O$ as the metal sources (Fig. 1a). SnS_xO_y or FeS_xO_y was also anchored on NF under the similar solvothermal environment, while $SnFeO_x$/NF was synthesized using urea as the metal precipitator. The representative SEM images of FeS_xO_y/NF (Fig. 1b) and SnS_xO_y/NF (Fig. 1c) reveal approximately spherical nanoparticles with average particle size of 500 nm on NF (Fig. S1), while the $SnFeS_xO_y$/NF shows much smaller nanoparticles with average particle size of 100 nm on NF surfaces (Fig. S2 and Fig. 1d and e), which endow the catalyst with large surface area and remarkable mass transport rate. TEM images also indicate larger nanoparticles in the FeS_xO_y/NF and SnS_xO_y/NF (Fig. S3) than in the $SnFeS_xO_y$/NF (Fig. 1f). From the HRTEM image (Fig. 1g), there are macrospores throughout the nanoparticles and the interplanar spacings of the $SnFeS_xO_y$ are 0.284 and 0.337 nm, characteristic of Fe- or Sn-containing oxides and sulfides. In addition, the crystals are very small, suggesting low degree of crystallinity in the $SnFeS_xO_y$. The elemental mappings of $SnFeS_xO_y$ display uniformly distributed O, S, Fe and Sn elements across the $SnFeS_xO_y$ surface (Fig. 2).

The valence states of Fe and Sn elements in the $SnFeS_xO_y$ are explored by XPS. As depicted in Fig. 3a, Fe, Sn, O and S elements are presented. The Fe $2p_{3/2}$ spectrum shows that two

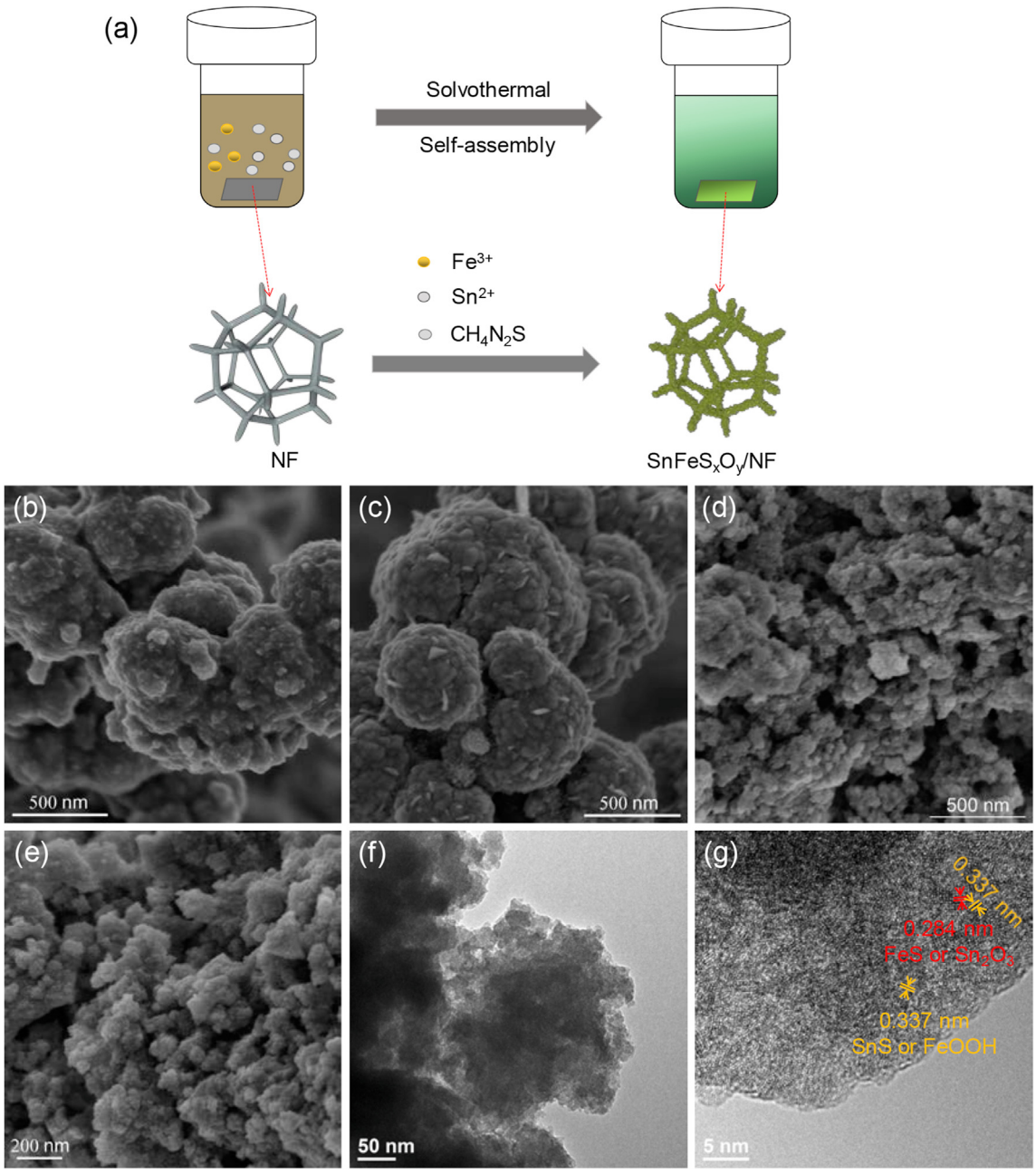

Fig. 1 – (a) Schematic of the synthesis of $SnFeS_xO_y$/NF. (b) SEM image of FeS_xO_y/NF. (c) SEM image of SnS_xO_y/NF. (d, e) SEM images of $SnFeS_xO_y$/NF. (f, g) HRTEM images of $SnFeS_xO_y$/NF.

significant peaks located at 710.9 and 713.1 eV correspond to Fe^{2+} and Fe^{3+} (Fig. 3b) [28]. The peak centered at 716.8 eV should be related to the Sn $3p_{3/2}$ [44]. The Sn 3d spectrum displays Sn $3d_{5/2}$ and Sn $3d_{3/2}$ peaks centered at 487.0 and 495.5 eV, respectively, indicating the presence of Sn^{4+} (Fig. 3c) [45]. The S 2p spectrum exhibits S $2p_{1/2}$ and S $2p_{3/2}$ peaks centered at 164.8 and 163.5 eV, respectively, corresponding to M – S species [46]. The O 1s spectrum can be fitted into three peaks center at 530.0, 531.5, and 532.5 eV, which can be ascribed to M – O (M = Fe or Sn), defective O sites and O–H, respectively (Fig. S4) [22].

The self-assembly oxysulfides on NF are directly served as working electrodes for electrocatalytic tests in N_2-saturated 1 M KOH. Fig. 4a demonstrates typical HER polarization curves of SnS_xO_y/NF, FeS_xO_y/NF, $SnFeO_x$/NF, $SnFeS_xO_y$/NF, and Pt/C/NF. The $SnFeS_xO_y$/NF needs a low overpotential (η_{10}) of 85 mV to reach 10 mA cm^{-2}, while SnS_xO_y/NF, FeS_xO_y/NF, $SnFeO_x$/NF and Pt/C/NF demand overpotentials of 98, 204, 178 and 33 mV respectively. Remarkably, the $SnFeS_xO_y$/NF needs low overpotentials of 167, 249, and 324 mV to reach 100, 500 and 1000 mA cm^{-2}, respectively, which surpasses most sulfides and oxyhydroxides reported previously (Table S1). Moreover, the $SnFeS_xO_y$/NF exhibits a Tafel slope of 90 mV dec^{-1} (Fig. 4b), lower than SnS_xO_y/NF (162 mV dec^{-1}) and $SnFeO_x$/NF (129 mV dec^{-1}), suggesting a favorable HER kinetics on the $SnFeS_xO_y$/NF. The Fe-doping content on the HER performance of

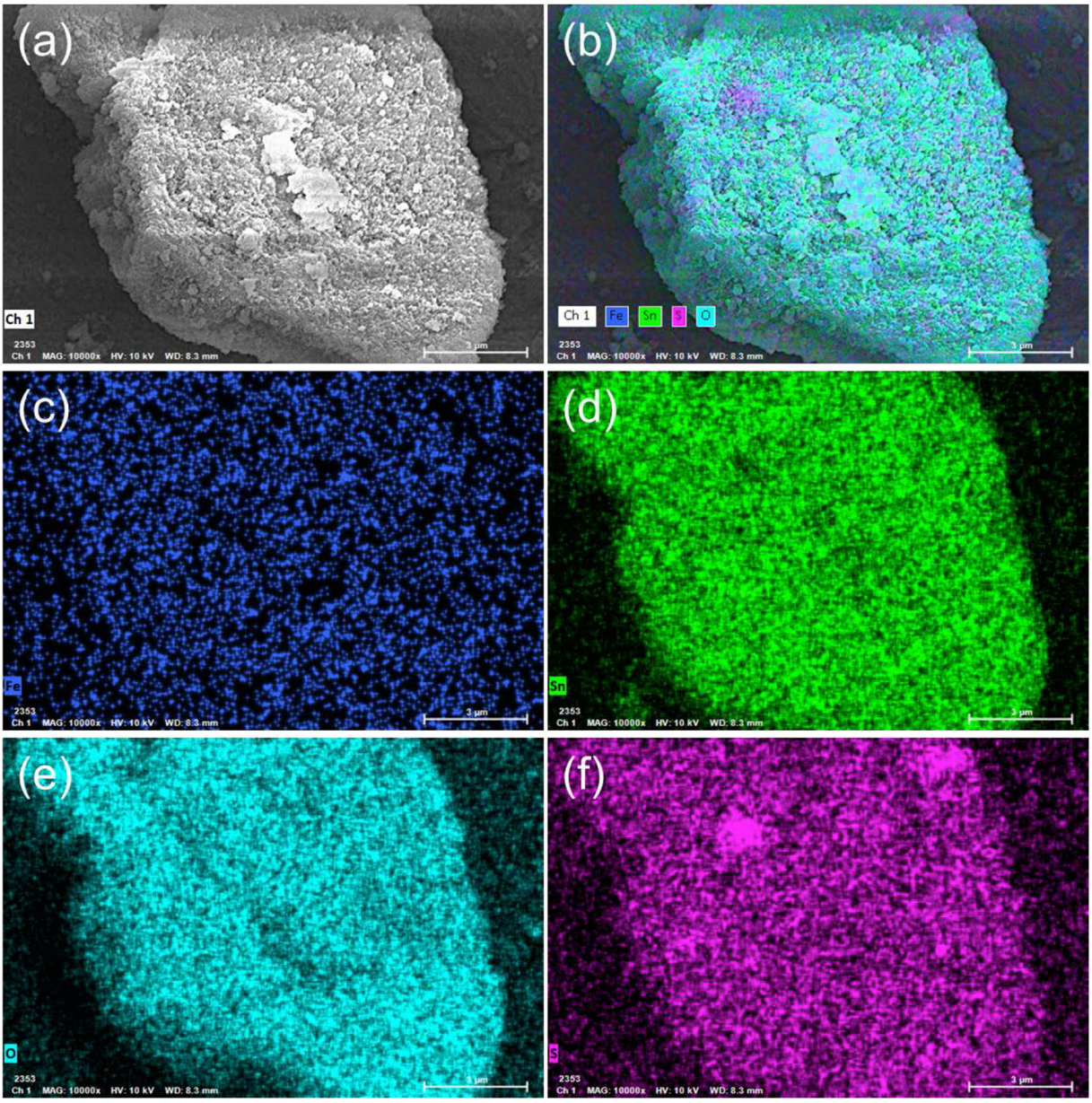

Fig. 2 – (a) SEM image of $SnFeS_xO_y$, and (b–f) elemental mapping.

$SnFe_nS_xO_y$/NF (n = 0.6–1.4) was investigated. As depicted in Fig. 4c, the Fe-doping content has great effect on the HER activity. The HER activity increases with augmenting Fe dosage and achieves a peak value when the Sn/Fe ration is 1:1. The HER activity will decrease gradually with further augmenting the Fe dosage. As a result, the η_{10} on $SnFe_{0.6}S_xO_y$/NF, $SnFe_{0.8}S_xO_y$/NF, $SnFeS_xO_y$/NF, $SnFe_{1.2}S_xO_y$/NF and $SnFe_{1.4}S_xO_y$/NF is 209, 131, 85, 178, and 227 mV (Fig. 4c), and their corresponding Tafel slopes are 127, 95, 90, 123, and 121 mV dec^{-1}, respectively (Fig. 4d). The long-term stability shows that the $SnFeS_xO_y$/NF maintains a well constant current density of 50 mA cm^{-2} for 54 h, indicating outstanding durability (Fig. 4e). The Faradaic efficiency of HER is measured to be ~100%. After the stability test at 50 mA cm^{-2} for 54 h, we collected the LSV curve (Fig. 4f), which indicates that there is no significant difference for the LSV curves before and after stability testing, further illustrating excellent HER stability of the $SnFeS_xO_y$/NF.

The catalytic OER performance of $SnFeS_xO_y$/NF is investigated in N_2-saturated 1 M KOH. For comparison, SnS_xO_y/NF, FeS_xO_y/NF, $SnFeO_x$/NF and commercial IrO_2 are also tested under the same conditions. The $SnFeS_xO_y$/NF achieves a current density of 100 mA cm^{-2} at an overpotential of only 281 mV (Fig. 5a), which is lower than that of the SnS_xO_y/NF (362 mV), FeS_xO_y/NF (318 mV), $SnFeO_x$/NF (310 mV), commercial IrO_2 (398 mV), and most sulfides and oxyhydroxides reported previously (Fig. 5b), for instance, CuCo–Ni_3S_2/NF (400 mV) [47], $CuInS_2/SnS_2$/NF (382 mV) [48], NiCoS/NF (370 mV) [49], VO_x/Ni_3S_2@NF (358 mV) [50], Bi–Ni_3S_2/NF (339 mV) [51], Zn–Ni_3S_2/NF (330 mV) [52], WS_x/Ni_9S_8/NF (320 mV) [53], MoS_x@$Co_9S_8Ni_3S_2$/NF (310 mV) [54], FeS–Ni_3S_2/

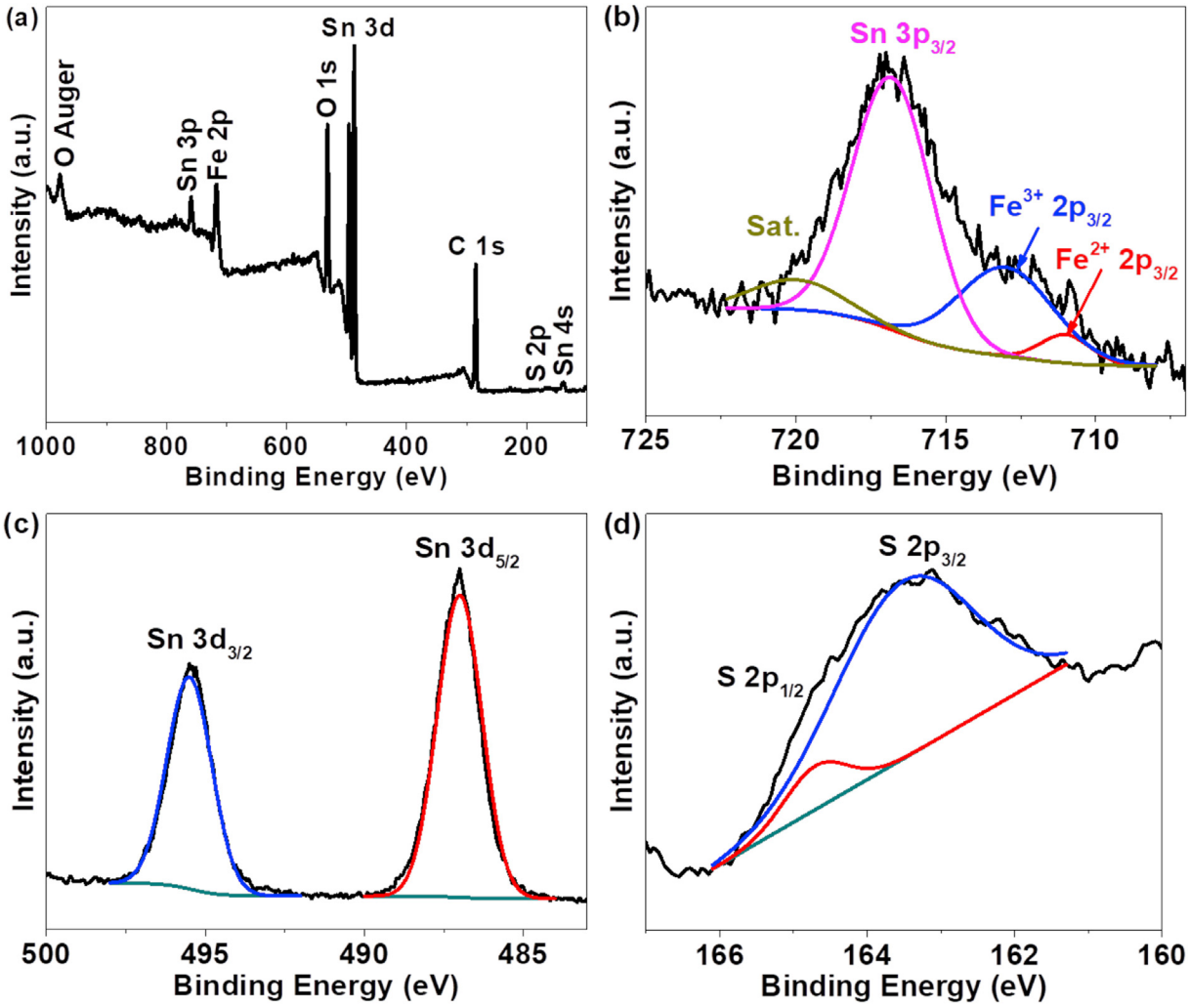

Fig. 3 – (a) XPS survey spectrum of the $SnFeS_xO_y$/NF. High-resolution XPS spectra for (b) Fe 2p, (c) Sn 3d and (d) S 2p.

NF (290 mV) [55], and Co_xP@Ni–Co–S/NF (289 mV) [56]. The turn over frequency (TOF) of oxygen evolution on the $SnFeS_xO_y$/NF at an overpotential of 300 mV is calculated to be 0.1 s^{-1} per total Fe and Sn atoms, far larger than SnS_xO_y/NF (0.026 s^{-1}), FeS_xO_y/NF (0.041 s^{-1}) and $SnFeO_x$/NF (0.039 s^{-1}). The mass activity of $SnFeS_xO_y$/NF at an overpotential of 300 mV is 189.3 A g^{-1}, much larger than SnS_xO_y/NF (50.0 A g^{-1}), FeS_xO_y/NF (77.7 A g^{-1}) and $SnFeO_x$/NF (82.2 A g^{-1}). The Tafel slope of $SnFeS_xO_y$/NF is 60 mV dec^{-1} (Fig. 5c), smaller than that of SnS_xO_y/NF (90 mV dec^{-1}), FeS_xO_y/NF (75 mV dec^{-1}), and $SnFeO_x$/NF (73 mV dec^{-1}), confirming the favorable OER kinetics of $SnFeS_xO_y$/NF and the rate-determining step following the first electron transfer [11]. The $SnFe_nS_xO_y$/NF samples with different Sn/Fe ratios (from 1:0.6 to 1:1.4) were also synthesized and investigated to optimize the OER performance. From Fig. 5d, the ratio of 1:1 exhibits better performance than the other analogues, verifying the fundamental positive influence of Fe^{3+}. The Tafel slope of $SnFe_{0.8}S_xO_y$/NF, $SnFeS_xO_y$/NF, $SnFe_{1.2}S_xO_y$/NF and $SnFe_{1.4}S_xO_y$/NF is 62, 60, 65 and 67 mV dec^{-1}, respectively (inset in Fig. 5d), suggesting similar OER mechanism on these samples. The OER kinetic barriers on SnS_xO_y/NF, FeS_xO_y/NF, $SnFeO_x$/NF and $SnFeS_xO_y$/NF were determined using Arrhenius equation [18,57]. From the temperature-dependent polarization curves (Fig. S5) and the derived Arrhenius plots (Fig. 5e), it can be calculated that the energy barrier on the $SnFeS_xO_y$/NF is 14.7 kJ mol^{-1}, much lower than that on SnS_xO_y/NF (23.1 kJ mol^{-1}), FeS_xO_y/NF (20.7 kJ mol^{-1}), and $SnFeO_x$/NF (19.1 kJ mol^{-1}), implying more favorable OER kinetics on the $SnFeS_xO_y$/NF.

The OER stability of $SnFeS_xO_y$/NF was evaluated by Chronopotentiometric and chronoamperometric meausrements (Fig. 5f). Both tests demonstrate that the $SnFeS_xO_y$/NF is very stable under high current density conditions, making $SnFeS_xO_y$/NF a promising OER catalyst. The Faradaic efficiency of OER is measured to be 95–100%. The structure and morphology of the $SnFeS_xO_y$/NF after OER stability test have been analyzed by XRD (Fig. S6) and SEM (Fig. S7), respectively. From Fig. S6, it can be seen that the species of sulfides and oxyhydroxides have been presented after OER testing, however, the morphology of the $SnFeS_xO_y$/NF after OER stability test is different from the fresh sample (Fig. S7). The particle size grows larger during OER testing, which might be due to surface and bulk reorganization during the reaction [11,20].

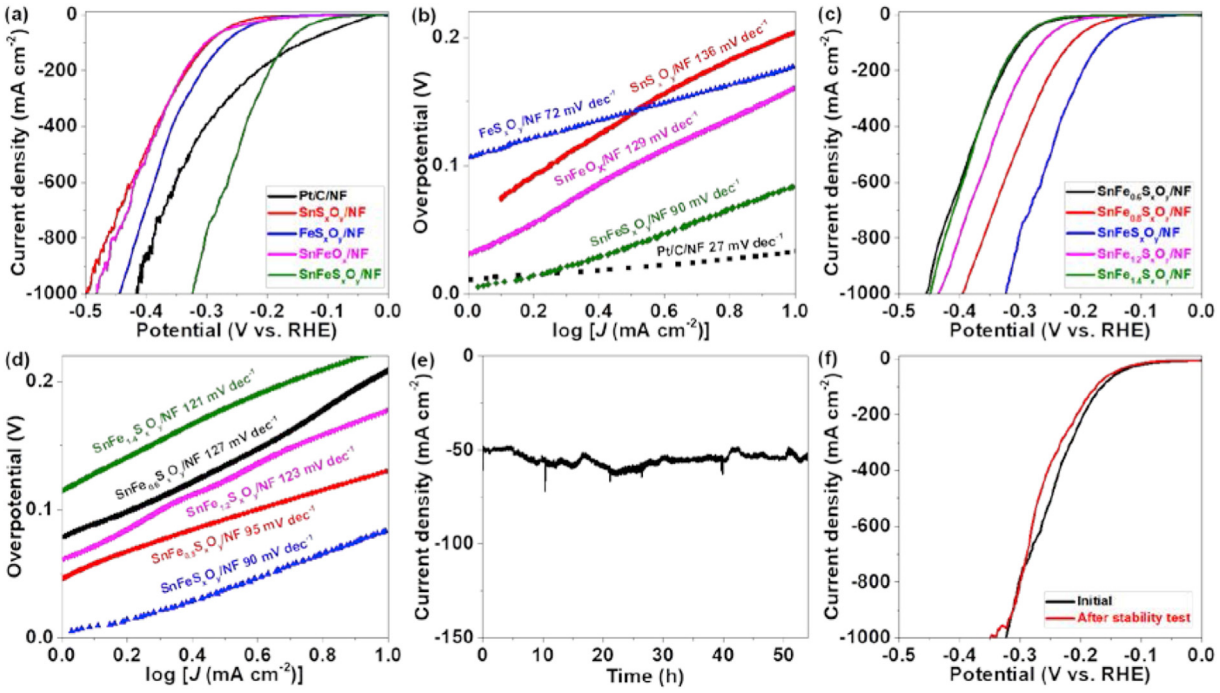

Fig. 4 – (a) LSV curves of Pt/C, SnS_xO_y/NF, FeS_xO_y/NF, $SnFeO_x$/NF and $SnFeS_xO_y$/NF. (b) Tafel plots. (c) LSV curves of $SnFe_{0.6}S_xO_y$/NF, $SnFe_{0.8}S_xO_y$/NF, $SnFeS_xO_y$/NF, $SnFe_{1.2}S_xO_y$/NF and $SnFe_{1.4}S_xO_y$/NF. (d) Tafel plots. (e) Chronoamperometric test for the $SnFeS_xO_y$/NF. (f) LSV curves of $SnFeS_xO_y$/NF before and after stability test.

The surface compositions and metal valence state of the $SnFeS_xO_y$/NF after OER measurement were analyzed by XPS. As depicted in Fig. S8, Fe, Sn, O and S elements can be still detected on the catalyst surface. Compared with fresh sample, the Fe^{2+}/Fe^{3+} ratio increases obviously, suggesting that Fe sites might be involved in the OER. Meanwhile, the Sn element

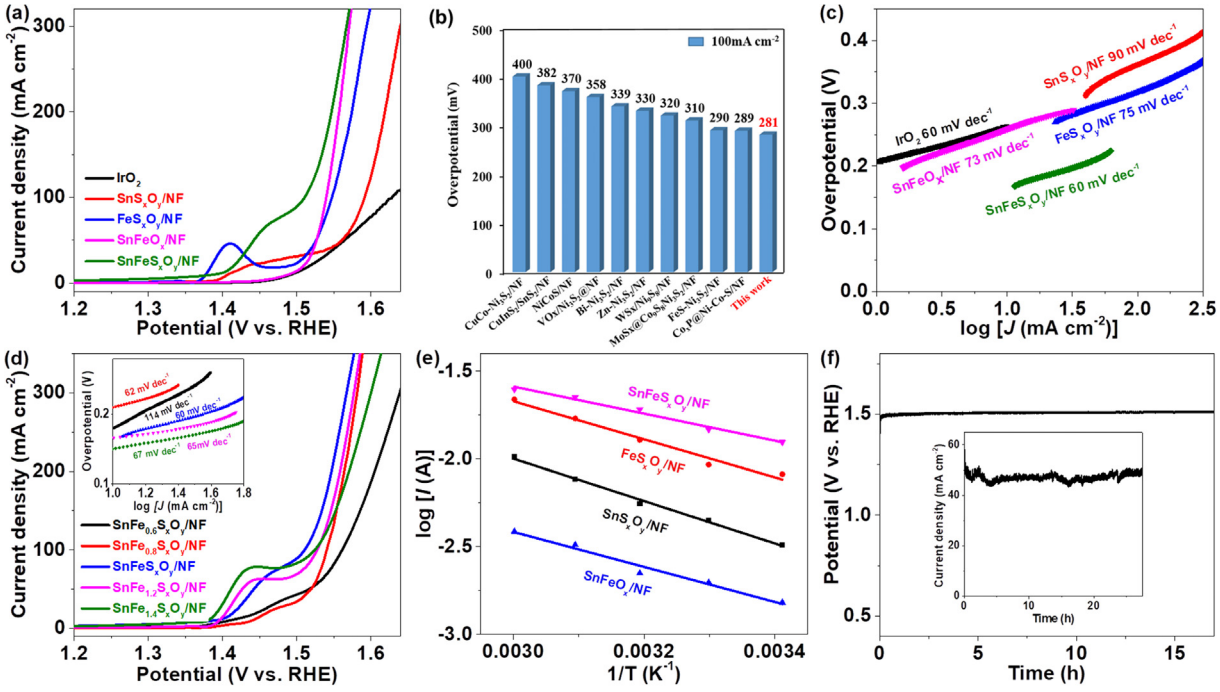

Fig. 5 – (a) LSV curves of IrO_2, SnS_xO_y/NF, FeS_xO_y/NF, $SnFeO_x$/NF and $SnFeS_xO_y$/NF. (b) Comparison of the overpotential at 100 mA cm^{-2}. (c) Tafel plots. (d) LSV curves of $SnFe_{0.6}S_xO_y$/NF, $SnFe_{0.8}S_xO_y$/NF, $SnFeS_xO_y$/NF, $SnFe_{1.2}S_xO_y$/NF and $SnFe_{1.4}S_xO_y$/NF. Inset: Tafel plots. (e) Arrhenius plots of the kinetic current at $\eta = 300$ mV. (f) Chronopotentiometric curve of the $SnFeS_xO_y$/NF (inset: chronoamperometric curve).

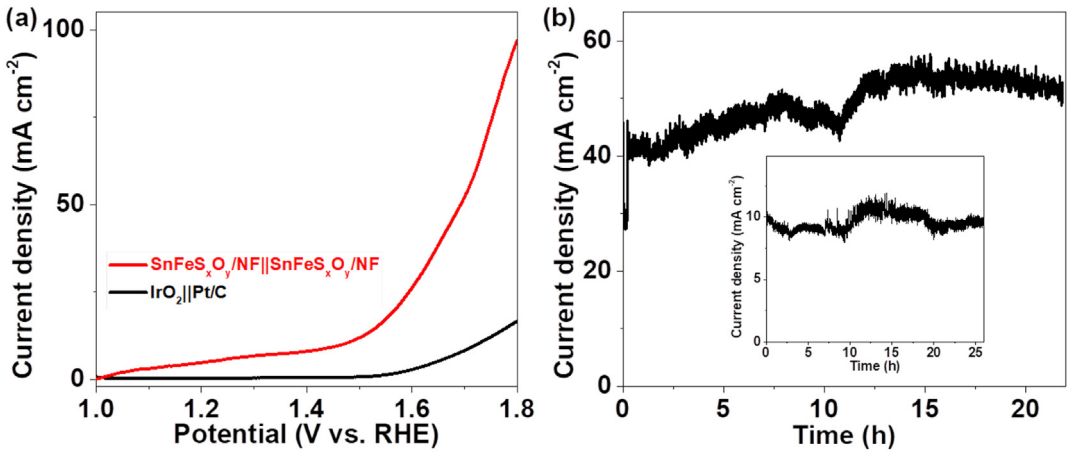

Fig. 6 – (a) LSV curves of overall water splitting. (b) Chronoamperometric test for the $SnFeS_xO_y$/NF||$SnFeS_xO_y$/NF at a cell voltage of 1.7 V (inset: the cell voltage is 1.5 V).

still remains +4 valence state after the reaction, implying that Sn should not be the main active site, but improves the conductivity and charge transfer ability as evidenced by the following impedance test.

To further disclose the role of Fe and Sn in the $SnFeS_xO_y$/NF for the HER and OER, the electrochemically active surface area (ECSA) was measured and compared with the other analogues. As shown in Figs. S9-S12, the ECSA of the $SnFeS_xO_y$/NF is 636 cm^2, much higher than SnS_xO_y/NF (393 cm^2), FeS_xO_y/NF (305 cm^2), and $SnFeO_x$/NF (47 cm^2), illustrating more available active sites in the $SnFeS_xO_y$/NF. The higher ECSA might come from two aspects: (1) the formation of heterostructure between the sulfides and oxyhydroxides, and (2) the synergistic effect between Sn and Fe sites increasing efficient active sites. Since the ECSA of $SnFeO_x$/NF is much lower than those of SnS_xO_y/NF and FeS_xO_y/NF, the heterostructure between the sulfides and oxyhydroxides in the $SnFeS_xO_y$/NF plays a more important role in enhancing the active sites. To investigate the influence of the formation of heterostructure on charge-transfer resistance, electrochemical impedance spectroscopy (EIS) spectra were performed. As illustrated in Figs. S13, the charge-transfer resistance of $SnFeS_xO_y$/NF is determined to be 2.1 Ω cm^2, slightly smaller than that of SnS_xO_y/NF (43.6 Ω cm^2), FeS_xO_y/NF (22.2 Ω cm^2) and $SnFeO_x$/NF (2.4 Ω cm^2), demonstrating that faster charge transfer in the $SnFeS_xO_y$/NF than the other samples.

Since the $SnFeS_xO_y$/NF exhibits excellent HER and OER activities, it shows enormous potential as cathode and anode materials for water electrolysis. Fig. 6a illustrates a typical polarization curve of an electrolytic cell that is assembled with the $SnFeS_xO_y$/NF as the cathode and anode. Evidently, the $SnFeS_xO_y$/NF||$SnFeS_xO_y$/NF electrolyzer provides the current density of 50 mA cm^{-2} at a low cell voltage of 1.69 V for the overall water splitting, outperforming the one assembled with nonprecious IrO_2||Pt/C. At the cell voltage of 1.8 V, the water-splitting output of this electrolyzer reaches ~96.8 mA cm^{-2}, 5.8-fold higher than the one constructed with IrO_2||Pt/C. The sulfides should be responsible for the HER, while the oxyhydroxides are responsible for the OER, and they are very stable for these reactions [15,58–60]. During the stability test at the voltages of 1.5 and 1.7 V, the output of the $SnFeS_xO_y$/NF||$SnFeS_xO_y$/NF electrolyzer is reasonably stable (Fig. 6b), implying potential applications of $SnFeS_xO_y$/NF for alkaline water electrolysis.

Conclusions

In summary, we have successfully assembled a heterostructure $SnFeS_xO_y$ onto nickel foam by a facile solvothermal synthesis to produce a bifunctional electrocatalyst for the overall water splitting. The $SnFeS_xO_y$/NF needs overpotentials of only 85, 167, 249, and 324 mV to reach 10, 100, 500 and 1000 mA cm^{-2} for the HER, respectively. Meanwhile, the $SnFeS_xO_y$/NF needs a low overpotential of only 281 mV to achieve a current density of 100 mA cm^{-2} for the OER. Additionally, the $SnFeS_xO_y$/NF can act as both anode and cathode to catalyze water electrolysis, requiring a low cell voltage of 1.69 V to deliver 50 mA cm^{-2}. The formation of Sn- and/or Fe-containing sulfide/oxyhydroxide heterostructure and the synergic action between Sn and Fe sites accelerate charge transfer and lower reaction barriers, thus improving electrocatalytic performance.

Declaration of competing interest

The authors declare that they have no known competing financial interests or personal relationships that could have appeared to influence the work reported in this paper.

Acknowledgments

This work was supported by and the Education Department of Jilin Province (No. JJKH20220967KJ), the Natural Science Foundation of Jilin Province (No. 20220101051JC), and the National Natural Science Foundation of China (No. 22075099).

Appendix A. Supplementary data

Supplementary data to this article can be found online at https://doi.org/10.1016/j.ijhydene.2022.11.039.

REFERENCES

[1] Tang T, Wang Z, Guan J. A review of defect engineering in two-dimensional materials for electrocatalytic hydrogen evolution reaction. Chin J Catal 2022;43:636–78.
[2] Shi L-N, Cui L-T, Ji Y-R, Xie Y, Zhu Y-R, Yi T-F. Towards high-performance electrocatalysts: activity optimization strategy of 2D MXenes-based nanomaterials for water-splitting. Coord Chem Rev 2022;469:214668.
[3] Bai X, Guan J. MXenes for electrocatalysis applications: modification and hybridization. Chin J Catal 2022;43:2057–90.
[4] Luo Y, Zhang Z, Chhowalla M, Liu B. Recent advances in design of electrocatalysts for high-current-density water splitting. Adv Mater 2022;34:2108133.
[5] Chatenet M, Pollet BG, Dekel DR, Dionigi F, Deseure J, Millet P, et al. Water electrolysis: from textbook knowledge to the latest scientific strategies and industrial developments. Chem Soc Rev 2022;51:4583–762.
[6] Ahsan MA, He T, Noveron JC, Reuter K, Puente-Santiago AR, Luque R. Low-dimensional heterostructures for advanced electrocatalysis: an experimental and computational perspective. Chem Soc Rev 2022;51:812–28.
[7] Tang Y, Yang C, Xu X, Kang Y, Henzie J, Que W, et al. MXene nanoarchitectonics: defect-engineered 2D MXenes towards enhanced electrochemical water splitting. Adv Energy Mater 2022;12:2103867.
[8] Guo T, Li L, Wang Z. Recent development and future perspectives of amorphous transition metal-based electrocatalysts for oxygen evolution reaction. Adv Energy Mater 2022;12:2200827.
[9] Tang T, Li S, Sun J, Wang Z, Guan J. Advances and challenges in two-dimensional materials for oxygen evolution. Nano Res 2022;15:8714–50.
[10] Chandrasekaran S, Khandelwal M, Dayong F, Sui L, Chung JS, Misra RDK, et al. Developments and perspectives on robust nano- and microstructured binder-free electrodes for bifunctional water electrolysis and beyond. Adv Energy Mater 2022;12:2200409.
[11] Guan J, Bai X, Tang T. Recent progress and prospect of carbon-free single-site catalysts for the hydrogen and oxygen evolution reactions. Nano Res 2022;15:818–37.
[12] Peng Y, Bai Y, Liu C, Cao S, Kong Q, Pang H. Applications of metal-organic framework-derived N, P, S doped materials in electrochemical energy conversion and storage. Coord Chem Rev 2022;466:214602.
[13] Yu Z-Y, Duan Y, Feng X-Y, Yu X, Gao M-R, Yu S-H. Clean and affordable hydrogen fuel from alkaline water splitting: past, recent progress, and future prospects. Adv Mater 2021;33:2007100.
[14] Li Y, Yin Z, Cui M, Liu X, Xiong J, Chen S, et al. Interface engineering of transitional metal sulfide-MoS2 heterostructure composites as effective electrocatalysts for water-splitting. J Mater Chem 2021;9:2070–92.
[15] Wang M, Zhang L, He Y, Zhu H. Recent advances in transition-metal-sulfide-based bifunctional electrocatalysts for overall water splitting. J Mater Chem 2021;9:5320–63.
[16] Li W, Wang C, Lu X. Integrated transition metal and compounds with carbon nanomaterials for electrochemical water splitting. J Mater Chem 2021;9:3786–827.
[17] Ifkovits ZP, Evans JM, Meier MC, Papadantonakis KM, Lewis NS. Decoupled electrochemical water-splitting systems: a review and perspective. Energy Environ Sci 2021;14:4740–59.
[18] Bai X, Duan Z, Nan B, Wang L, Tang T, Guan J. Unveiling the active sites of ultrathin Co-Fe layered double hydroxides for the oxygen evolution reaction. Chin J Catal 2022;43:2240–8.
[19] Han J, Zhang M, Bai X, Duan Z, Tang T, Guan J. Mesoporous Mn-Fe oxyhydroxides for oxygen evolution. Inorg Chem Front 2022;9:3559–65.
[20] Han J, Guan J. Multicomponent transition metal oxides and (oxy) hydroxides for oxygen evolution. Nano Res 2022. https://doi.org/10.1007/s12274-022-4874-7.
[21] Bai X, Ma Y, Wang Q, Guan J. Core-shell Ni3Fe-based nanocomposites for the oxygen evolution reaction. Int J Hydrogen Energy 2022;47:2304–12.
[22] Bai X, Fan Y, Hou C, Tang T, Guan J. Partial crystallization of Co-Fe oxyhydroxides towards enhanced oxygen evolution activity. Int J Hydrogen Energy 2022;47:16711–8.
[23] Huang W, Li J, Liao X, Lu R, Ling C, Liu X, et al. Ligand modulation of active sites to promote electrocatalytic oxygen evolution. Adv Mater 2022;34:2200270.
[24] Hua W, Sun H, Jiang M, Ren L, Zhang Y, Wang J-G. Cascading reconstruction to induce highly disordered Fe-Ni(O)OH toward enhanced oxygen evolution reaction. J Mater Chem 2022;10:7366–72.
[25] Cheng B, Kong K, Zhang L, Sa R, Gu T, Rui Y, et al. Accelerating water oxidation kinetics via synergistic in-layer modification and interlayer reconstruction over hetero-epitaxial Fe-Mn-O nanosheets. Chem Eng J 2022;441:136122.
[26] Inamdar AI, Chavan HS, Hou B, Lee CH, Lee SU, Cha S, et al. A robust nonprecious CuFe composite as a highly efficient bifunctional catalyst for overall electrochemical water splitting. Small 2020;16:1905884.
[27] Fan K, Ji Y, Zou H, Zhang J, Zhu B, Chen H, et al. Hollow iron-vanadium composite spheres: a highly efficient iron-based water oxidation electrocatalyst without the need for nickel or cobalt. Angew Chem Int Ed 2017;56:3289–93.
[28] Chakraborty B, Beltrán-Suito R, Hausmann JN, Garai S, Driess M, Menezes PW. Enabling iron-based highly effective electrochemical water-splitting and selective oxygenation of organic substrates through in situ surface modification of intermetallic iron stannide precatalyst. Adv Energy Mater 2020;10:2001377.
[29] Sahoo DP, Das KK, Mansingh S, Sultana S, Parida K. Recent progress in first row transition metal Layered double hydroxide (LDH) based electrocatalysts towards water splitting: a review with insights on synthesis. Coord Chem Rev 2022;469:214666.
[30] Li X-P, Huang C, Han W-K, Ouyang T, Liu Z-Q. Transition metal-based electrocatalysts for overall water splitting. Chin Chem Lett 2021;32:2597–616.
[31] Zhang Q, Guan J. Applications of single-atom catalysts. Nano Res 2022;15:38–70.
[32] Li S, Li E, An X, Hao X, Jiang Z, Guan G. Transition metal-based catalysts for electrochemical water splitting at high current density: current status and perspectives. Nanoscale 2021;13:12788–817.
[33] Fu Q, Han J, Wang X, Xu P, Yao T, Zhong J, et al. 2D transition metal dichalcogenides: design, modulation, and challenges in electrocatalysis. Adv Mater 2021;33:1907818.
[34] Liu X, Jiang X, Shao G, Xiang H, Li Z, Jin Y, et al. Activating the electrocatalysis of MoS2 basal plane for hydrogen evolution via atomic defect configurations. Small 2022;18:2200601.
[35] Yi L, Ji Y, Shao P, Chen J, Li J, Li H, et al. Scalable synthesis of tungsten disulfide nanosheets for alkali-acid electrocatalytic sulfion recycling and H-2 generation. Angew Chem Int Ed 2021;60:21550–7.

[36] Heift D. Iron sulfide materials: catalysts for electrochemical hydrogen evolution. INORGA 2019;7:75.
[37] Tian B, Kolodziejczyk W, Saloni J, Cheah P, Qu J, Han F, et al. Intercalation of cobalt cations into Co9S8 interlayers for highly efficient and stable electrocatalytic hydrogen evolution. J Mater Chem 2022;10:3522–30.
[38] He W, Liu H, Cheng J, Li Y, Liu C, Chen C, et al. Modulating the electronic structure of nickel sulfide electrocatalysts by chlorine doping toward highly efficient alkaline hydrogen evolution. ACS Appl Mater Interfaces 2022;14:6869–75.
[39] Zhou G, Shan Y, Wang L, Hu Y, Guo J, Hu F, et al. Photoinduced semiconductor-metal transition in ultrathin troilite FeS nanosheets to trigger efficient hydrogen evolution. Nat Commun 2019;10:399.
[40] Li S, Sun J, Guan J. Strategies to improve electrocatalytic and photocatalytic performance of two-dimensional materials for hydrogen evolution reaction. Chin J Catal 2021;42:511–56.
[41] Yin J, Jin J, Zhang H, Lu M, Peng Y, Huang B, et al. Atomic arrangement in metal-doped NiS2 boosts the hydrogen evolution reaction in alkaline media. Angew Chem Int Ed 2019;58:18676–82.
[42] Yan Y, Wang P, Lin J, Cao J, Qi J. Modification strategies on transition metal-based electrocatalysts for efficient water splitting. J Energy Chem 2021;58:446–62.
[43] Guo Y, Park T, Yi JW, Henzie J, Kim J, Wang Z, et al. Nanoarchitectonics for transition-metal-sulfide-based electrocatalysts for water splitting. Adv Mater 2019;31:1807134.
[44] Fondell M, Gorgoi M, Boman M, Lindblad A. An HAXPES study of Sn, SnS, SnO and SnO2. J Electron Spectrosc Relat Phenom 2014;195:195–9.
[45] Ji Z, Liu J, Deng Y, Zhang S, Zhang Z, Du P, et al. Accurate synergy effect of Ni–Sn dual active sites enhances electrocatalytic oxidation of urea for hydrogen evolution in alkaline medium. J Mater Chem 2020;8:14680–9.
[46] Liu F, He W, Li Y, Wang F, Zhang J, Xu X, et al. Activating sulfur sites of CoS2 electrocatalysts through tin doping for hydrogen evolution reaction. Appl Surf Sci 2021;546:149101.
[47] Qin J-F, Yang M, Hou S, Dong B, Chen T-S, Ma X, et al. Copper and cobalt co-doped Ni3S2 grown on nickel foam for highly efficient oxygen evolution reaction. Appl Surf Sci 2020;502:144172.
[48] Guo Z, Yang F, Zhang B, Wang X, Liu Z. In situ formed CuInS2/SnS2 hybrid on foam-like nickel as bifunctional electrode for water splitting. Electrochim Acta 2022;405:139802.
[49] Yan K-L, Shang X, Li Z, Dong B, Chi J-Q, Liu Y-R, et al. Facile synthesis of binary NiCoS nanorods supported on nickel foam as efficient electrocatalysts for oxygen evolution reaction. Int J Hydrogen Energy 2017;42:17129–35.
[50] Niu Y, Li W, Wu X, Feng B, Yu Y, Hu W, et al. Amorphous nickel sulfide nanosheets with embedded vanadium oxide nanocrystals on nickel foam for efficient electrochemical water oxidation. J Mater Chem 2019;7:10534–42.
[51] Du B, Luo Y, Liu G, Xue W, Wang Y, Li J, et al. P-block Bi doping stabilized reconstructed nickel sulfide as high-performance electrocatalyst for oxygen evolution reaction. Electrochim Acta 2022;426:140779.
[52] Liu Q, Xie L, Liu Z, Du G, Asiri AM, Sun X. A Zn-doped Ni3S2 nanosheet array as a high-performance electrochemical water oxidation catalyst in alkaline solution. Chem Commun 2017;53:12446–9.
[53] Ma X, Zhang X-Y, Yang M, Xie J-Y, Lv R-Q, Chai Y-M, et al. High-pressure microwave-assisted synthesis of WSx/Ni9S8/NF hetero-catalyst for efficient oxygen evolution reaction. Rare Met 2021;40:1048–55.
[54] Feng X, Jiao Q, Zhang J, Cui H, Li H, Zhao Y, et al. Integrating amorphous molybdenum sulfide nanosheets with a Co9S8@Ni3S2 array as an efficient electrocatalyst for overall WaterSplitting. Langmuir 2022;38:3469–79.
[55] Wu F, Guo X, Hao G, Hu Y, Jiang W. Synthesis of iron-nickel sulfide porous nanosheets via a chemical etching/anion exchange method for efficient oxygen evolution reaction in alkaline media. Adv Mater Interfac 2019;6:1900788.
[56] Li M, Zheng K, Zhang J, Li X, Xu C. Design and construction of 2D/2D sheet-on-sheet transition metal sulfide/phosphide heterostructure for efficient oxygen evolution reaction. Appl Surf Sci 2021;565:150510.
[57] Swierk JR, Klaus S, Trotochaud L, Bell AT, Tilley TD. Electrochemical study of the energetics of the oxygen evolution reaction at nickel iron (Oxy)Hydroxide catalysts. J Phys Chem C 2015;119:19022–9.
[58] Lin L, Sherrell P, Liu Y, Lei W, Zhang S, Zhang H, et al. Engineered 2D transition metal dichalcogenides-A vision of viable hydrogen evolution reaction catalysis. Adv Energy Mater 2020;10:1903870.
[59] Hao Y, Li Y, Wu J, Meng L, Wang J, Jia C, et al. Recognition of surface oxygen intermediates on NiFe oxyhydroxide oxygen-evolving catalysts by homogeneous oxidation reactivity. J Am Chem Soc 2021;143:1493–502.
[60] Song F, Bai L, Moysiadou A, Lee S, Hu C, Liardet L, et al. Transition metal oxides as electrocatalysts for the oxygen evolution reaction in alkaline solutions: an application-inspired renaissance. J Am Chem Soc 2018;140:7748–59.